Design and efficiency modelling of a fixed-ratio hydraulic transformer

Pierre Bernard and Vincent Langlois

Poclain Hydraulics Industrie, Verberie, France
E-mail: pierre.bernard@poclain.com, vincent.langlois@poclain.com

Abstract

A hydraulic transformer, sometimes also described as a pressure booster or pressure amplifier, is a component used to transform a hydraulic power, from a flow Q1 and pressure P1 to another state of flow Q2 and pressure P2. The pressure booster's aim is usually to multiply the pressure level by a given ratio, thus dividing the amount of flow by the same ratio. Common challenges in such components are transformation efficiency, outlet pressure and outlet flow dynamics, and space claim.
The present work investigates the design and modelling of a – compact – fixed ratio pressure amplifier based on a radial pistons cam-lobe architecture. This type of architecture has been used for years in direct drive mobile and industrial applications, and its technology is here adapted to a hydraulic transformer concept.
The component's concept and design are described along with its basic kinematic and dynamic behaviour. Then, models of the hydromechanical and volumetric losses are presented, allowing the complete simulation of the power transformation's efficiency. A confrontation of the efficiency modelling with experimental results constitutes the last part of the paper, showing good agreement of simulated results with measurements on a prototype version of the pressure intensifier. The model developed in this work can be used to vary design parameters, and optimise the design of the pressure amplifier to maximize the efficiency of the power transformation.

Keywords: Hydraulic transformer, pressure booster, radial pistons, cam-lobe, efficiency

1 Introduction

In a context of global drive towards energy economy, there is a need for hydrostatic transmissions and hydraulic systems to evolve towards more efficient architectures and components [1, 2]. The general trend of electrification of the prime mover, replacing diesel engines, puts a focus on uptime of the machines, also pushing towards greater system efficiency. One way for hydrostatic transmissions to get more efficient is to move to higher pressure levels. Indeed, increasing pressure will lower the required displacement for a given torque, which will allow a reduction of flow in the system, thus lowering pressure drops and increasing the transmission's overall efficiency. However, as shown by Achten in [3], the maximum rated pressure in hydraulic systems has not changed for the past 40 years, and despite a few components available for higher pressure levels [4, 5], no ecosystem of components is yet available to move to the next level of pressure.
To make a step in the direction of increased pressure, Poclain proposed a concept of boosted radial pistons cam-lobe motor [6, 7], which incorporates a pressure amplifier. This boosted motor is able to internally increase its working pressure beyond that of the hydraulic system when the need arises, thus allowing a reduction in the installed displacement. The present work investigates the concept of the pressure amplifier used in the proposed boosted motor. Indeed, although several different concepts of pressure amplifiers have been proposed along the years, see for example [8–11], including it inside a hydraulic motor to amplify the pressure without impacting the rest of the system is - to the best of the authors' knowledge - a novelty.
Amplifying the pressure in the hydraulic circuit of a mobile application, or directly inside a hydraulic motor poses some challenges, which existing pressure boosters do not meet. Indeed, in a hydraulic motor directly driving a machine's wheel, pressure and flow ripples can easily be felt by the machine's operator, as they are directly creating a jerky behaviour on the machine's movement, and can also lead to vibrations and noise. The amplification ratio and inlet pressure level are also quite specific, and no commercially available amplifier was found that met the criteria. Finally, the space claim of existing pressure boosters is quite important, and integrating them inside a motor that must fit in a wheel is not easy. This is to try and solve these shortcomings that the radial pistons cam-lobe pressure booster has been designed. This paper will first describe the basic design and kinematics of the concept. The second part of the paper is dedicated to the modelling of losses

and efficiency of the proposed concept, while the final part discusses the results of the efficiency modelling, and compares experimental results with simulations. In a further work, the models presented in this paper will be used to improve and optimise the design of the component, to maximize the efficiency of the power transformation.

2 A radial pistons cam-lobe pressure amplifier

In this first section, the concept and patented [12] design of the radial pistons cam-lobe pressure booster (RPCLB) are presented.

2.1 Concept

The RPCLB uses radial pistons with two separate pushing stages in order to create a motor and a pump in the same rotating group. Figure 1 shows a schematic view of the operating principle of the RPCLB, in which the top stage of the piston (or head) is used as a motor, while the lower stage (or foot) is used as a pump. In fig. 1, the orange colour indicates high system pressure HP_{sys} which is the inlet pressure to the booster, the blue colour is low system pressure LP_{sys} which is also the pressure on the secondary outlet port of the device, and the red colour is the amplified pressure on the RPCLB's outlet HP_{boost}. Due to the difference in pressurised areas between the motoring and the pumping stages of the pistons, the pressure is amplified from HP_{sys} to HP_{boost}.

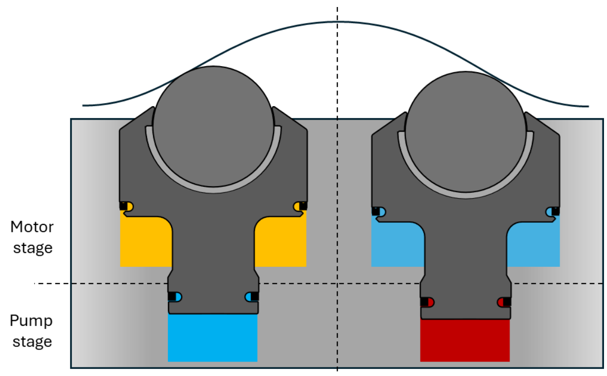

Figure 1: RPCLB *operating principle*

2.2 Design and parameters

The specific design of the RPCLB in this study is composed of 3 pistons and 4 cam-lobes, as illustrated by fig. 2. The ratio of displacements of the two parts (motor and pump) is 3.27, with a motor displacement of 34.9 cc/rev, and a pump displacement of 10.7 cc/rev. Figure 2 introduces the different elements composing the torque module of the RPCLB. The cam (1) is fixed, and as the cylinder-block (2) rotates, the pistons (3), pushed by pressurised fluid, move in and out of their bore in a direction radial to the cylinder-block. As this movement occurs, the cylindrical rollers (4) roll along the cam profile, their rotation movement with respect to the pistons being facilitated by the bushings (5). Sealing rings (6, 7) define two fluid volumes under each piston, both volumes alternately suck in fluid during the outwards stroke of the piston, and discharge fluid during the inwards stroke. Although the rotation of the cylinder-block is described as counter-clockwise on fig. 2, the RPCLB is perfectly capable of rotating in clockwise direction, thus reducing pressure to increase flow output. In the design studied in this

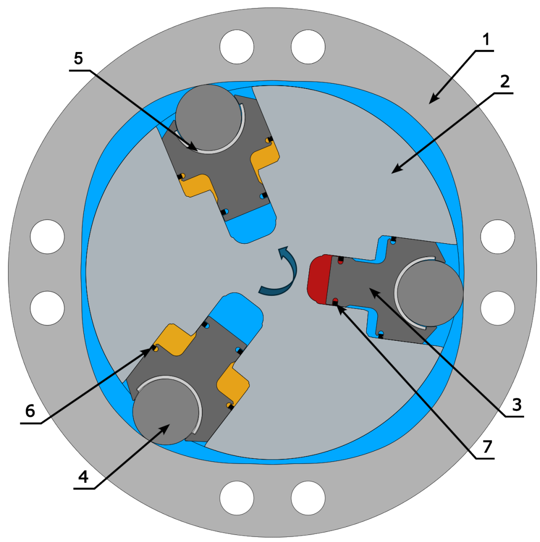

Figure 2: RPCLB *operating principle*

work, the case of the RPCLB is linked to the low pressure port P_3 of the amplifier (see fig. 3), which means that the case is subjected to the low system pressure (symbolised by the blue colour between cylinder-block and cam on fig. 2). Because of this case pressurisation, the net hydraulic force applied on the piston is the force due to the pressures in the two piston chambers, to which is subtracted the force due to the pressure in the case.

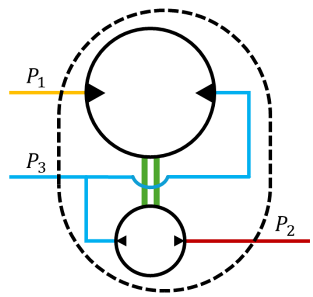

Figure 3: RPCLB *schematic representation*

3 Modelling

In this section, the kinematics of the RPCLB is described, and models of hydrodynamic and volumetric losses are presented in order to obtain a model of the energetic transformation occurring in the component.

3.1 Kinematics

Figure 4 represents one piston with the parameters describing the cam profile and roller coordinates, as well as the different forces at play. As the roller rolls along the cam profile, contacting it in a point described by the (α, R_{CRC}) coordinates, its centre follows a trajectory described by the (θ, ρ) coordinates.

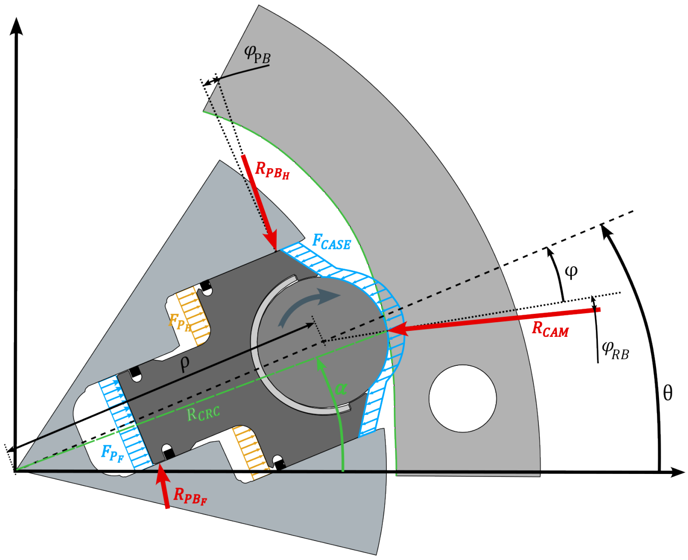

Figure 4: RPCLB *kinematics, and piston force balance*

The direction normal to the cam-roller contact forms an angle φ with the piston axis.

The laws of motion (speed V_P, and acceleration Γ_P) of the piston in its bore can directly be derived from the trajectory of the roller centre.

$$V_P(\theta) = \frac{d\rho}{dt} = \frac{d\rho}{d\theta} \cdot \omega \tag{1}$$

$$\Gamma_P(\theta) = \frac{d^2\rho}{dt^2} = \frac{d^2\rho}{d\theta^2} \cdot \omega^2 \tag{2}$$

The fluid flow displaced by each chamber of a piston (Q_{Pist_M};Q_{Pist_P}) are derived from eq. (1, 2), and the sum of volumes displaced by all pistons then gives the motor and pump stages volume displacements (D_M;D_P).

$$Q_{Pist_M} = V_P \cdot \frac{\pi({D_{P_h}}^2 - {D_{P_f}}^2)}{4}; D_M = \sum_{N_P} Q_{Pist_M} \tag{3}$$

$$Q_{Pist_P} = V_P \cdot \frac{\pi {D_{P_f}}^2}{4}; D_P = \sum_{N_P} Q_{Pist_P} \tag{4}$$

In equations (3, 4), the quantities D_{P_h} and D_{P_f} represent the diameters of the head and tail of the piston. The theoretical pressure amplification ratio $r_{amp_{th}}$ is defined as the ratio of the motor and pump stages displacement, as given by eq (5).

$$r_{amp_{th}} = \frac{D_M}{D_P} \tag{5}$$

3.2 Internal forces

The equipped piston force balance is illustrated on fig. 4, with the different reaction forces R_{PB_H}, R_{PB_F}, and R_{CAM}, resulting from the pressure forces applied to the piston F_{P_H}, F_{P_F}, and F_{CASE}. The force balance equation of the equipped piston is represented by eq. (6), applied at the centre of the roller.

$$\begin{pmatrix} 0 \\ F_{P_H} + F_{P_F} - F_{CASE} \\ 0 \end{pmatrix} = \left[M\right] \begin{Bmatrix} R_{CAM} \\ R_{PB_H} \\ R_{PB_F} \end{Bmatrix} \tag{6}$$

The matrix $\left[M\right]$ accounts for distances from force application points to roller centre, and for the angles φ_{PB} and φ_{RB} which are related to friction coefficients in a way described in §3.3.2. A more detailed description of the piston force balance, albeit applied to a standard piston design instead of the stepped piston of the RPCLB can be found in [13]. In the RPCLB, a rotary planar distributor is used to distribute the pressurised fluid to the piston chambers at the appropriate time, in the same way as on radial pistons cam lobe motors. The principle and simulation of such a valve is detailed in [14]. The friction losses in such a distributor valve are low, thanks to the total separation of surfaces by the fluid film. However, to balance the forces in the film, an axial counter-balance force is needed. This force F_{dist} directed from the valve to the cylinder-block, is created by the differential sections of valve grooves, and is transferred through the cylinder-block to the tapered roller bearing, as illustrated on fig. 5.

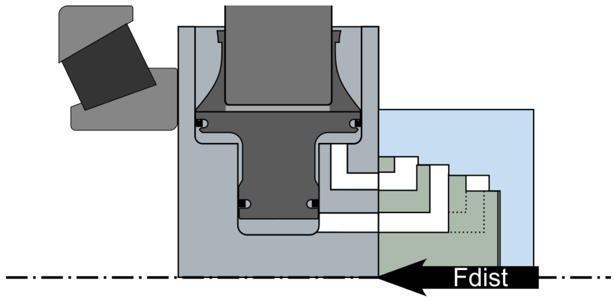

Figure 5: Distribution force impact on the bearing

3.3 Hydromechanical losses model

In order to correctly evaluate the transformation ratio of the RPCLB, both the hydromechanical and volumetric losses must be taken into account. Hydromechanical losses relate to losses having an impact on the amount of torque generated by a motor, or the torque required by a pump to generate a given flow at a certain pressure level. These losses can further be broken down into pressure drops and friction related losses.

3.3.1 Pressure drops

Due to the tortuous geometry of the channelling in the distribution part of the RPCLB, the minor head losses (pressure losses due to perturbations in the channels: bends, convergents, divergence,. . .) dominate the major head losses (pressure losses that occur along the length of pipes or channels) in the component. These minor head losses can be calculated using eq. (7), in which ρ_{oil} is the oil density, ξ is a coefficient related to the geometry, and V_{fluid} is the oil speed in the reference area corresponding to the pressure drop coefficient ξ.

$$\Delta p = \frac{1}{2}\rho_{oil}\xi V_{fluid}^2 \tag{7}$$

The pressure drop in the different parts of the oil distribution channels is taken into account as a succession of orifices. Figure 6 illustrates the different orifices used to represent the pressure drop along the path of the fluid. Four valve channels are represented, linked to the RPCLB's inlet port P_1 by a circular channel usually referred to as a groove. The modelling is

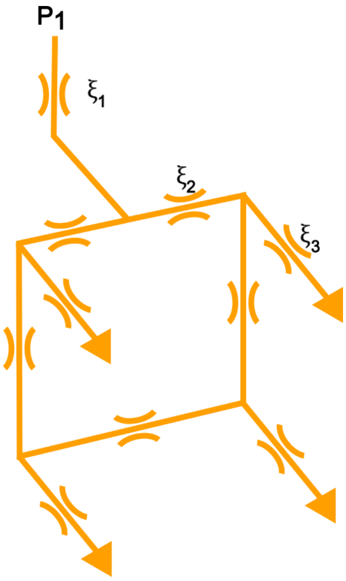

Figure 6: Inlet groove representation for pressure drops calculation

identical for the two outlet ports $P_2$and P_3. On fig. 6, three coefficients are noted, as the pressure drop coefficient for all channels ξ_3 are identical, and the pressure drop coefficient ξ_2 is the same for all orifices along the groove. The oil flow rate entering at port P_1 is equal to the sum of the oil flow rates exiting at the four valve channels (as symbolised by the arrows on fig. 6).From these, and the pressure drop coefficients ξ_i and corresponding flow areas of the groove, the conservation of mass flow allows the calculation of the flow in each of the areas, and thus the global pressure drop between port P_1 and each of the valving ports.
The modelling of pressure losses in the cylinder-block's channels is done in a similar way. However, at the interface of the cylinder-block and valve channels, the planar distributor requires a special modelling. Indeed, the flow passage area at the interface between each valve channel and cylinder-block drilling, defined as the intersection of the cylinder-block and valve orifices, varies with the angular position of the cylinder-block, as illustrated in fig. 7. For this reason, eq. (7) is adapted for this calculation and becomes eq. (8), where $A(\theta)$ is the flow passage area at the valving interface for a given valve and cylinder-block orifice couple.

$$\Delta p(\theta) = \frac{1}{2}\rho_{oil}\xi(\theta)\left(\frac{Q_{Pist}(\theta)}{A(\theta)}\right)^2 \tag{8}$$

It should also be noted, that due to the evolving flow passage area, the pressure drop coefficient $\xi(\theta)$ at this interface is also variable.

3.3.2 Friction losses

There are three main sources of frictional loss in the RPCLB.

Roller/Bushing friction The interface between the roller and

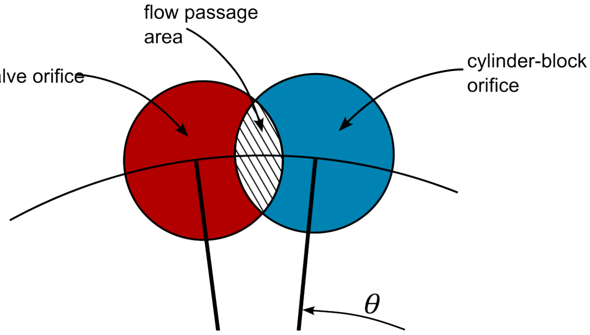

Figure 7: Valving interface flow passage area

bushing can be described as a partial arc journal bearing. The sliding motion is facilitated by the bushing's plastic material in low speed conditions, and a hydrodynamic fluid film separates the surfaces in higher-speed operation conditions. A semi-empirical model is used, building upon elementary test results realised on a radial pistons cam lobe motor. This model relates the friction coefficient to the Sommerfeld number defined by eq. (9), and leads to friction coefficient values shown in fig. 8. A particularity that is not captured by the standard Stribeck curve is a higher dependence on the load applied to the contact. In fact, the load parameter P^* is experimentally found to have an impact on friction coefficient, beyond the Sommerfeld parameter. This is due to the pressure-induced deformation of the bushing, which tends to increase the friction coefficient at lower loads, and which would require an elasto-hydrodynamic modelling approach, coupling parts deformation and fluid film pressure to be simulated accurately. Due to simulation running time concerns, and scope of the work, this is not attempted here, and the Stribeck curve model is adapted to reflect the pressure dependence induced by deformations. Hence, several curves appear on fig. 8, to highlight this stronger pressure dependence.

$$S = \frac{\mu \cdot V}{p^*} \tag{9}$$

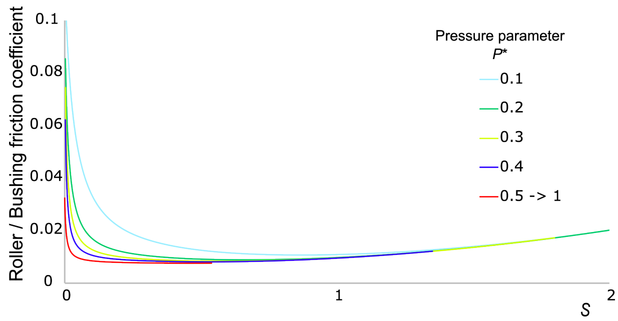

Figure 8: Pressure dependent Stribeck curves for the Roller/Bushing friction coefficient cof_{RB}

Using the friction coefficient given in fig. 8, the friction force in the roller/bushing contact can easily be obtained as the product of the friction coefficient cof_{RB},and the theoretical roller/bushing reaction. However, the model does not calculate friction individually, but rather uses the friction coefficient in the global piston force balance of eq. 6. To that effect, the angle φ_{RB} is calculated through eq. 10.

$$\varphi_{RB} = atan(cof_{RB}) \tag{10}$$

Piston/Cylinder friction In the same way, the piston/bore contact friction is modelled using a semi-empirical model based on the Sommerfeld number of eq. (9), where V now stands for the piston sliding speed $V_P(\theta)$. It must be noted that since the piston has a reciprocating motion in its bore, it constantly travels up and down the Stribeck curve of fig. 9. An additional particularity is that since the maximum piston sliding speed remains low compared to the roller/bushing sliding speed, the Sommerfeld number remains low, and the curve does not show a re-increase of the coefficient of friction at higher Sommerfeld values, indicating that the hydrodynamic regime is never reached. In a similar manner to the roller/bushing friction described previously, the angle φ_{PB} is obtained by way of eq. 11, and subsequently used in eq. 6.

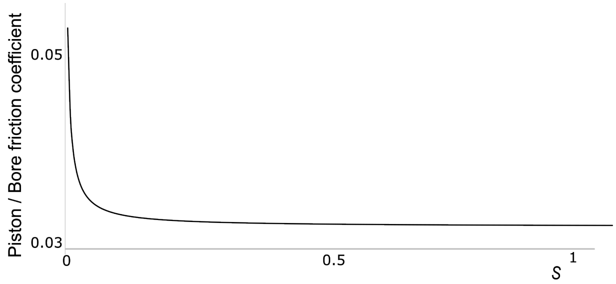

Figure 9: Stribeck curve for the Piston/Bore friction coefficient cof_{PB}

$$\varphi_{PB} = atan(cof_{PB}) \tag{11}$$

Bearing internal friction In addition to the two previous friction sources, the RPCLB includes a third main source of frictional loss in the bearings, which is much more significant in the booster design than it is in a radial pistons camlobe motor. The reason for the significance of the losses in the bearing is due to the higher speeds that can be reached by the RPCLB, and also to the fact that the net torque on the rotor of the RPCLB is zero, so any torque loss in the bearing results in a lower pressure amplification ratio. Bearings modelling and losses have been a subject of study for many years, and good engineering models are proposed by suppliers (see for example [15], and [16]). For the purposes of this study, because of its easy implementation, and the availability of the required parameters and equations, the SKF model [16] is used. It is an analytical model, which calculates frictional moment with the inputs of geometry, rotation speed and axial and radial forces on the bearing.

3.4 Volumetric losses model

The volumetric losses in the RPCLB are mostly internal leakages, as the leakage flow can only follow a limited number of paths:

- From high pressure (port P_1) to low pressure (port P_3).
- From boosted pressure (port P_2) to low pressure (port P_3).
- From boosted pressure (port P_2) to high pressure (port P_1).

These losses happen at different locations of the RPCLB, but the vast majority of the leakage flow is concentrated at the piston sealing rings (6, 7) on fig.2). An empirical model is used to relate leakage flow to oil sealing ring differential pressure and fluid viscosity. Indeed the leakage flow through an individual sealing ring is found to be linearly correlated to the pressure level, and the effect of piston sliding speed is very limited when looking at leakage values averaged over one RPCLB revolution.

$$Q_{leak} = \alpha_r \cdot \Delta p \cdot \nu^{0.4} \tag{12}$$

Equation (12) is used in the model to calculate the leakage flow through an individual sealing ring. In this equation, α_r is a constant determined by the sealing ring type, and ν is the kinematic viscosity of the hydraulic fluid. The individual leakage flows through the different sealing rings are summed in order to obtain the leakage flow through each of the three paths described previously.
In addition to these leakage flows, the compressibility of the fluid also leads to a volumetric inefficiency, which can be assimilated to an internal leakage flow. Compressibility losses impact fluid volumes that see a switch between pressure levels. In the RPCLB, this is the case of the oil volume contained in the cylinder-block, between the valving interface and the bottom surface of the piston, as illustrated on fig. 10 for the piston's foot.

$$\Delta V = \frac{V_0 \cdot \Delta p}{\beta} \tag{13}$$

This volume switches from boosted to low pressure N_L times per revolution.

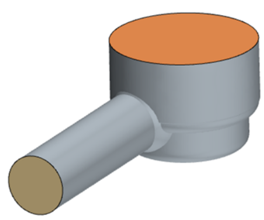

Figure 10: Dead volume under the piston's foot

Using eq.(13), the volume that is lost due to compressibility effects can be calculated. It is then transformed in a volumetric flow rate by multiplying the value of ΔV by $N_L \times L_P = 12$ times (due to the $N_L = 4$ commutation events for each of the $N_P = 3$ pistons) the rotation speed. In a similar manner, there is a volumetric flow rate that can be calculated, corresponding to the head part of the piston, where the pressure switches from low to high at bottom dead centre (where the oil volume under the piston is $V_{0,H}$, or dead volume under the piston's head), and from high to low at top dead centre (where the oil volume under the piston is $V_{D,H}$, which is the volume displaced by the head part of the piston). Taking into account the compressibility effects leads to the well known *p-V* diagrams depicted in fig.11 for the motoring cycle (orange), and the pumping cycle (red).

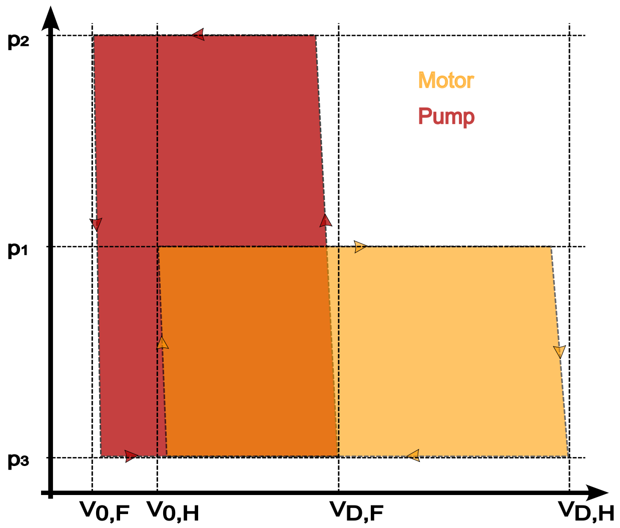

Figure 11: p-V diagram for motor and pump cycles

3.5 Complete simulation

Putting together all the individual bricks presented in the previous sections allows the simulation of the behaviour of the RPCLB for a given set of inlet conditions (flow, pressure and temperature), and low pressure setting. The complete simulation process is described in fig. 12. After convergence of the

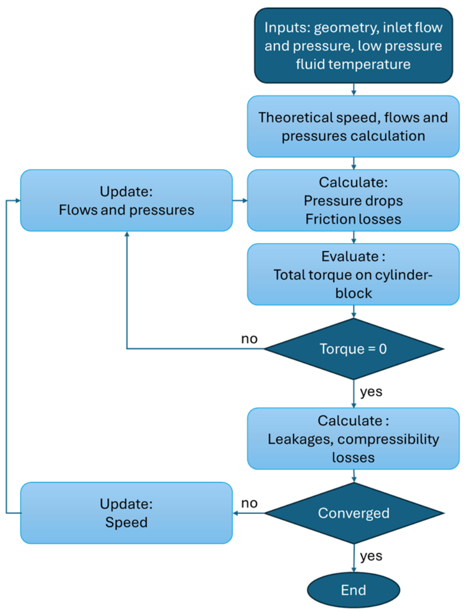

Figure 12: Complete simulation process

pressure and flow values on the RPCLB's outlet ports P_2, and P_3, the pressure amplification ratio, the ratio of outlet (P_2) flow over inlet (P_1) flow , and the global transformation efficiency can be calculated. In addition to these average values, some angle dependant values can also be interesting. Indeed, the simulation model is able to output the flow and pressure values in function of the cylinder-block's angular position, therefore allowing a calculation of flow and pressure stability metrics.

4 Results and discussion

4.1 Transformation ratio

The transformation efficiency links the increase of pressure to the reduction of flow rate, as seen from P_1 to P_2. This efficiency is calculated with the help of eq. (14).

$$\eta_{trans} = \frac{p_{P_2} \cdot Q_{P_2}}{p_{P_1} \cdot Q_{P_1}} \tag{14}$$

Figure 13 shows the transformation efficiency map for the RPCLB, as defined by eq. 14, in function of the pressure and flow at the inlet port P_1, under a hydraulic fluid inlet temperature of $50°C$, and a low pressure on the outlet port P_3 set to 20 bar. Figures 14,15 respectively show the corresponding pressure increase ratio, equal to p_{P_2} over p_{P_1}, and the flow rate at the outlet port P_2.

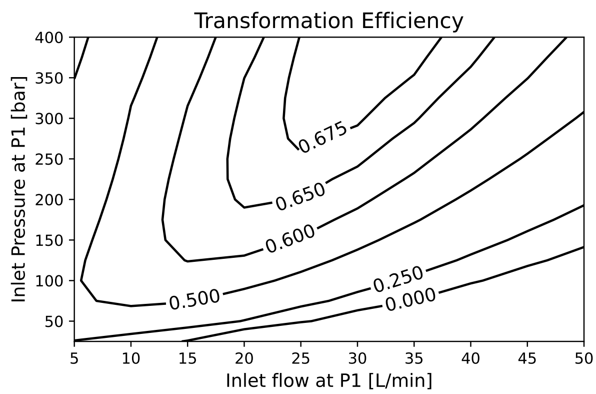

Figure 13: Overall transformation efficiency η_{trans}

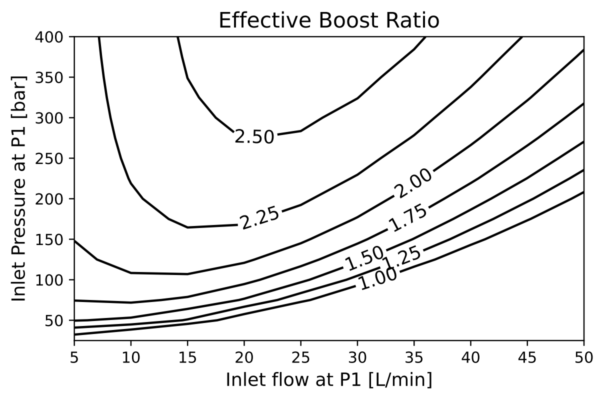

Figure 14: Effective pressure increase ratio $(p_{P_2} \div p_{P_1})$

4.2 Valid operating conditions

The transformation efficiency map of fig.13 shows that the efficiency can be equal to zero in some conditions of high inlet flow and low inlet pressure. In addition, fig.14 also displays ratios lower than one in a slightly more extended zone.

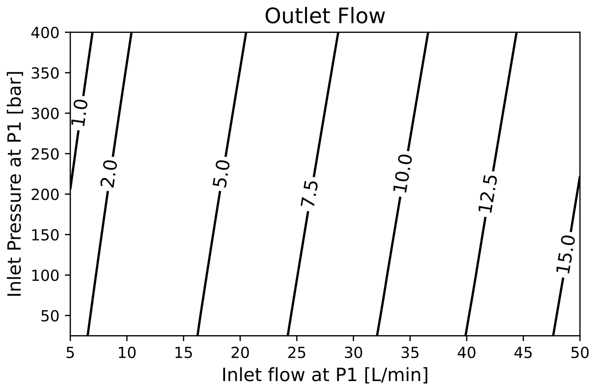

Figure 15: Outlet flow Q_{P_2} (L\min)

This clearly defines operating conditions where the RPCLB is – at best – counter-productive, and perhaps even inoperable. Figure 16 shows in a red zone the operating conditions where

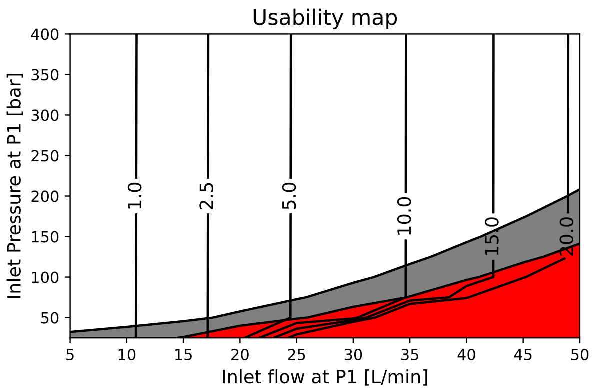

Figure 16: Possible operating conditions of RPCLB

the RPCLB is inoperable, and in grey the operating conditions where it is counter-productive, and the outlet pressure at port P_2 is actually lower than the inlet pressure at port P_1. Superimposed on these coloured areas, are contour lines indicating the minimum pressure requirement on the outlet port P_3 to ensure that no cavitation occurs inside the component.

4.3 Flow stability

Using the simulation model, it is also possible to investigate the variations of outlet flow during one rotation of the RPCLB's cylinder-block. Indeed, as explained in §1, the flow variation on the outlet line of the pressure amplifier is an important criterion for the pressure booster. The outlet flow variation can be calculated by the developed simulation model, and shows low values of flow ripple. The variation is in the range of $\pm 3\%$ of the nominal flow value, which is a good improvement on the pulsating outlet flow that is created by standard – commercially available – pressure amplifier. Figure 17 compares the outlet flow, plotted in function of time, for a commercially available pressure amplifier and the RPCLB in identical conditions: 200bar inlet pressure and 20L/min inlet flow.

As shown by fig. 17, the RPCLB shows a much lower flow

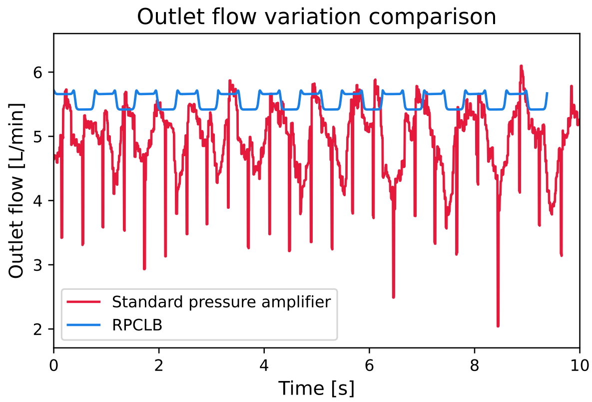

Figure 17: Comparison of simulated RPCLB *and measured commercially available pressure booster outlet flow. 200 bar and 20L/min inlet*

ripple than the standard pressure amplifier, making it a better fit for integration in a the hydrostatic transmission of a mobile application.

4.4 Experimental results comparison

The design of RPCLB presented in this paper, and simulated by the model has been fabricated and tested on an elementary test bench (fig. 18). The inlet flow at port P_1 is controlled,

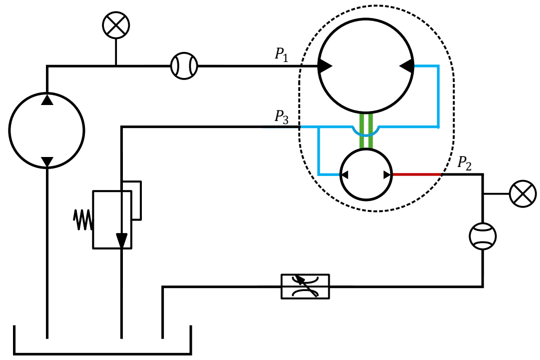

Figure 18: Elementary RPCLB *test bench setup*

and the pressure on the outlet port P_2 is set using a variable orifice. Due to test bench limitations, the boosted pressure level is limited to 450 bar. Figures 19, and 20 respectively show the outlet pressure and flow at port P_2, comparing simulated and measured values. The value of inlet pressure (at port P_1) is indicated by way of a colour scale, and the dots are simulated points, whereas the '$\times$' markers represent the measured points. For both the outlet pressure and flow, the simulation shows reasonably good agreement with the measured data. The difference between simulated and measured values, in percent, as calculated by eq. (15), is listed in tab. 1.

$$error_{\%} = 100 \times \frac{\overline{x}_{sim} - \overline{x}_{exp}}{\overline{x}_{exp}} \tag{15}$$

The simulation model correctly captures the overall trends of the RPCLB's volumetric and mechanical efficiencies. It can be

Table 1: Simulated vs measured value errors

error in %	pressure	flow
min	-8.64	-3.13
max	6.62	1.32
average	-1.28	-0.43

noted that the model seems to underestimate the outlet pressure for low flow values, which could indicate that the friction losses in the boundary lubrication regime are in fact lower than expected. As indicated in §3.3.2 the friction models for roller-bushing and piston-cylinder are based on measurements made on a radial pistons cam lobe motor of similar design to the RPCLB. However the pistons and rollers of the RPCLB are slightly smaller than their existing counterparts of the motor range, and some size effects could lead to this overestimation of boundary lubrication friction levels. Alternately, the real friction of the tapered roller bearing could be less than the SKF model predicts for low rotation speeds, as this kind of engineering model is more suited to higher speed operations commonly encountered by bearings.

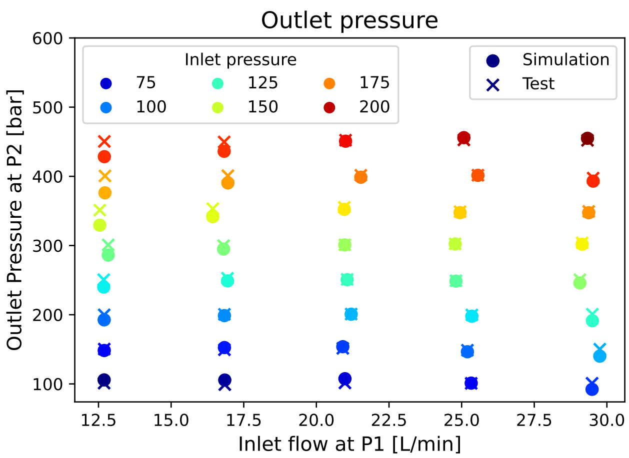

Figure 19: Comparison of simulated and measured outlet pressure

5 Conclusions and next steps

In this work, a concept of radial pistons cam lobe pressure intensifier is introduced, and a simulation model is described, which allows the calculation of outlet pressure and flow for given inlet conditions. The different parts of the model are described, accounting for hydromechanical and volumetric losses. Different outputs of the model are detailed, showing the amplification ratio, the transformation efficiency, and highlighting the limits in operating conditions. The simulation results are shown to be in good agreement with experimental results, with some possible modelling improvements to be made in the low flow regions.

The first tests realised on the RPCLB, and the simulation results, have shown a potential for improvements in the design of the component. In fact this was to be expected, as the tested version of the component is a preliminary design, with un-optimised parts and fabrication processes. The target was to have a functional component, and to evaluate it in light of the model. The simulation model will now be utilised to vary design parameters, in order to optimise the pressure intensifier's efficiency. The size and number of pistons, the size of the channels inside the RPCLB, as well as the internal distribution of fluid can be modified in the model to investigate the effect on outlet flow and pressure, and ultimately, to optimise its overall efficiency.

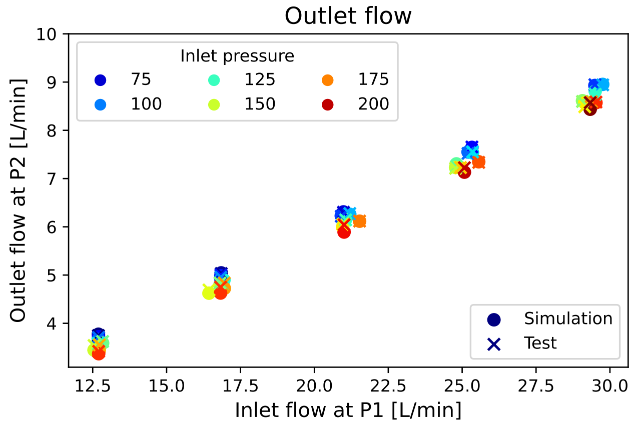

Figure 20: Comparison of simulated and measured outlet flow

Nomenclature

Symbol	**Description**
N_L	Number of lobes
N_P	Number of pistons
HP_{sys}	High system pressure
LP_{sys}	Low system pressure
HP_{boost}	Amplified pressure
D_{P_h}	Piston diameter (head)
D_{P_f}	Piston diameter (foot)
R_r	Roller radius
L_P	Piston total length
θ	Angular position
ρ	Roller centre position
α	Cam-roller contact point angular position
R_{CRC}	Cam-roller contact radial position
φ	Cam-roller contact incidence angle vs piston axis
ω	Rotation speed
V_P	Piston radial speed
Γ_P	Piston radial acceleration
R_{CAM}	Roller/Cam reaction force
R_{PB_H}	Piston/Bore contact force - piston head
R_{PB_F}	Piston/Bore contact force - piston foot
φ_{PB}	Piston/Bore friction coefficient

φ_{RB}	Roller/Bushing friction coefficient
β	Bulk modulus of the hydraulic fluid
P_1	1^{st} port of the RPCLB
P_2	2^{nd} port of the RPCLB
P_3	3^{rd} port of the RPCLB
Q_{Pist_M}	Flow for each piston in the motor stage
Q_{Pist_P}	Flow for each piston in the pump stage
D_M	Motor displacement
D_P	Pump displacement
$r_{amp_{th}}$	Theoretical amplification ratio
F_{P_H}	Pressure in piston's head chamber
F_{P_F}	Pressure in piston's foot chamber
F_{CASE}	Case pressure
F_{dist}	Distribution valve axial pushing force
Δ_P	Pressure drop
ρ_{oil}	Hydraulic fluid density
ξ	Pressure drop coefficient
V_{fluid}	Fluid speed in reference flow area
ξ_1	Inlet/Outlet pressure drop coefficient
ξ_2	Pressure drop coefficient in grooves flow area
ξ_3	Pressure drop coefficient in valve channel flow area
$Q_{Pist}(\theta)$	Piston flow requirement at a given angular position
$A(\theta)$	Flow passage area at interface
S	Sommerfeld number
μ	Oil dynamic viscosity
V	Oil speed in reference area
p^*	Pressure parameter for friction coefficient model
Q_{leak}	Leakage flow
V_0	Dead volume under piston
$V_{0,H}$	Dead volume under piston's head
$V_{D,H}$	Dead and displaced volume under piston's head
$V_{0,F}$	Dead volume under piston's foot
$V_{D,F}$	Dead and displaced volume under piston's foot
η_{trans}	Transformation efficiency
p_{P_1}	Pressure at port P_1
p_{P_2}	Pressure at port P_2
Q_{P_1}	Flowrate at port P_1
Q_{P_2}	Flowrate at port P_2
$error_{\%}$	Simulation result error compared to measurement
$\bar{x}_{sim}$	Simulated value
$\bar{x}_{exp}$	Measured value

References

[1] Thomas Heeger, Samuel Kärnell, and Liselott Ericson. Challenges for multi-quadrant hydraulic piston machines. *Energy Conversion and Management: X*, 22:100578, April 2024.

[2] Damiano Padovani, Pavlos Dimitriou, and Tatiana Minav. Challenges and solutions for designing Energy-Efficient and Low-Pollutant Machines in Off-Road hydraulics. *Energy Conversion and Management: X*, 21:100526, January 2024.

[3] Peter Achten. Innovation in the fluid power industry. *IFK Aachen*, 2014.

[4] HAWE. Radial piston pump type R, RG product documentation, 2024. [Accessed 2025-02-14].

[5] Poclain. MHP20/MHP27 Hydraulic Motors technical catalog, 2024. [Accessed 2025-02-14].

[6] Pierre Bernard, Vincent Langlois, and Maxime Maurer. Improving transmission efficiency via a novel radial piston cam lobe motor architecture. *Proc. of the 2024 International Maha Fluid Power Conference*, pages 20–38, 2024.

[7] Poclain. Advanced drive technology. *IVT Off-Highway Annual 2025*, pages 54–56, 2025.

[8] G M Barrett. Fluid pressure intensifier, 1973. Patent GB1317742A.

[9] Hammelmann Paul. Hydraulic pressure transformer, 1983. US Patent US4401415A.

[10] Feng Wang, Linyi Gu, and Ying Chen. A hydraulic pressure-boost system based on high-speed on-off valves. *IEEE-ASME Transactions on Mechatronics*, 18(2):733–743, 2013.

[11] Peter Achten. The design of the FCT80 hydraulic transformer. In *SICFP'23*, Tampere,Finland, June 2023.

[12] Gilles Lemaire, Yoann Rousseau, and Paul Fournet. Machine hydraulique multicylindrees amelioree, 2024. Patent WO2024231635A1.

[13] Chao Zhang, Hao Tan, Yu Fang, Xiaolong Zhang, Yu Yang, Yiman Duan, Min Han, Shaojian Cui, Bing Xu, and Junhui Zhang. Deformation pre-compensated optimization design of cam ring for low pulsation hydraulic motors. *Journal of Zhejiang University-SCIENCE A*, 24(2):130–145, 2023.

[14] Leon Dahlén and Peter Carlsson. Numerical optimization of a distributor valve. *International Journal of Fluid Power*, 4(3):17–25, November 2003.

[15] Schaeffler Technologies AG & Co. KG. Rolling bearings technical - principles and product data for the design of rolling bearing arrangements. pages 56–61, 2020. [Accessed 2025-02-03].

[16] SKF. The SKF model for calculating the frictional moment. 2009. [Accessed 2025-01-06].